

Properties of the Hermean regolith: II. Disk-resolved multicolor photometry and color variations of the "unknown" hemisphere

J. Warell

*Institutionen för Astronomi och Rymdfysik, Uppsala Universitet, Box 515, SE-751 20 Uppsala, Sweden
E-mail: johan.warell@astro.uu.se, Telephone: +46 18 471 5970, Fax: +46 18 471 5999*

Address editorial correspondence and proofs to:

J. Warell

ABSTRACT

Multicolor photometric observations of the "unknown" hemisphere of Mercury have been performed with the Swedish Vacuum Solar Telescope on La Palma at maximal elongations from the Sun in 1997 and 1998. A set of six interference filters with central wavelengths from 450 nm to 940 nm were used. Multicolor photometry of Mercury was performed on disk-resolved images of the "unknown" hemisphere (longitudes 160° – 340°) with a highest resolution of ~ 200 km (Warell & Limaye 2001).

Disk-integrated spectrophotometry shows that (1) the spectrum of Mercury displays a linear slope from 650 to 940 nm, indicating that the average mercurian regolith is considerably more mature than relatively immature pure anorthosite regions on the Moon; (2) there is negative evidence for the presence of the putative 1-micron absorption feature near 940 nm due to the presence of ferrous iron (Fe^{2+}) in pyroxenes; (3) no effect of phase reddening of the integrated disk is observed between phase angles of 63° and 84° .

For the first time, disk-resolved spectrophotometry of Mercury's surface has been obtained, from which it is inferred that (4) the scattering properties of Mercury's regolith are more homogeneous than for the Moon and that there is no clear relation between reflectance and chemical properties at spatial scales of ~ 300 km on the "unknown" hemisphere; (5) there exists an inverse relation of spectral slope with emission angle which is larger for Mercury than for the Moon, indicating that the average mercurian regolith is more backscattering and that this effect increases with wavelength.

Finally, from filter ratio images of Mercury's disk it is found that (6) no color variations larger than 2% with respect to the surroundings are detected at a spatial resolution of ~ 300 km.

Keywords: Mercury; Regoliths; Surfaces, Planets; Terrestrial planets; Spectrophotometry

1. Introduction

For the past forty years, numerous attempts have been made by different authors to gain knowledge of the compositional and scattering properties of Mercury's regolith by means of ground-based multicolor photometric, spectroscopic, polarimetric and radar studies. Due to the great difficulties imposed on such observations by the presence of Earth's atmosphere and Mercury's small angular distance to the Sun, results have often been unambiguous and contradictory. There is a common understanding today that the upper surface layer of Mercury's regolith has a very mature, agglutinitic and silicate-rich composition. Attempts at determining the mineralogical constituents have however not been completely convincing, although a large number of possible species have been indicated by the obtained data.

The vis-NIR spectral slope of Mercury is consistent with a mature lunar highland-like anorthositic surface, dominated by silicate mineralogy. Spectrophotometric and spectroscopic observations of the integrated disk (Harris 1961, Irvine et al. 1968, McCord & Adams 1972, Vilas & McCord 1976, Vilas et al. 1984, Vilas 1985) have not resulted in any unambiguous detections of spectral absorption features. Thermal infrared spectroscopy and imaging have indicated a surface containing pyroxenes, feldspars, ultra-mafic rocks and possibly basalt (Sprague et al. 1994, Jeanloz et al. 1995, Sprague et al. 1997, Sprague et al. 1998, Sprague et al. 2000). Locations with low-iron basalt are consistent with results from recalibrated Mariner 10 image data (Robinson & Lucey 1997). Though radar observations have provided topographic profiles (Clark et al. 1988, Harmon & Campbell 1988) and information on the optical properties of the regolith conforming to a low content of opaque phases such as ilmenite and magnetite (Jeanloz et al. 1995), little specific information concerning Mercury's mineralogical and chemical

composition has been obtained.

In this paper new multicolor photometry based on high-resolution CCD imaging with the Swedish Vacuum Solar Telescope (SVST; Warell & Limaye 2001) of the "unknown" (i.e. poorly known with respect to coverage by Mariner 10) hemisphere of Mercury is presented. A disk-integrated spectrum with a linear slope is obtained (Section 4), contributing negative evidence for the plausible ferrous "1-micron" absorption feature at a wavelength of 900–1000 nm. Disk-resolved photometry (Section 5) reveals feature spectra with higher slopes than typical lunar highland regolith, indicating a more mature surface. There is a strong inverse correlation on spectral slope with emission angle, suggesting that the mercurian regolith is more strongly backscattering, with increasing backscattering efficiency towards longer wavelengths, than that of the most mature lunar soil samples measured in the laboratory. A color ratio image analysis (Section 6) puts an upper limit on the intensity variations at the wavelength of the ferrous band of less than 2% at spatial scales of ~ 300 km. It is furthermore concluded that a detailed investigation of the scattering properties, for all possible ranges of illumination and viewing geometry, of available planetary geologic materials under Mercury-like conditions is probably vital to the understanding of Mercury's regolith.

2. Data acquisition

The acquisition and reduction of image data analysed in this paper has been discussed in detail by Warell & Limaye (2001) and will thus not be repeated here. Photometric analysis has been performed for data acquired in 1997 and 1998, obtained with identical instrumental setups, covering mainly the poorly known hemisphere of Mercury. In the present analysis, images subjected to basic darkframe and flatfield processing only has been used. The reduction of the photometric data sets is discussed in Section 3 below. The reader is referred to Warell & Limaye (2001)

for a description of the instrumental setup, the physical aspect of Mercury at the times of observation and albedo feature identifications.

3. Photometric observations and calibration

The photometric calibration of the Mercury images was performed in the following manner. The atmospheric extinction coefficients were calculated from calibration star observations by the Boguer method (Sterken & Manfroid 1992), and applied to Mercury flux measurements to obtain its instrumental extra-atmospheric flux in each filter band. The Mercury spectrum uncorrected for the calibration star and solar contributions was thus obtained. The calibration star spectrum was removed by first normalizing the Mercury spectrum at a wavelength of 830 nm, then dividing it by the stellar spectrum, also normalized at 830 nm. The fully reduced Mercury spectrum was then obtained from division by the similarly normalized solar spectrum. The spectra of the calibration stars were obtained from different sets of absolutely calibrated (i.e., telluric line absorptions removed) flux spectra from published spectrophotometry (see Appendix). The solar spectrum was obtained from spectrophotometry of the solar analog 16 Cygni B and a modelled solar continuum, as detailed in the Appendix.

3.1. Mercury observations

Photometry of Mercury was obtained for three dates at which calibration star observations were performed. On November 22 1997, calibration observations were made with Ealing interference filters (FWHM 36–63 nm) centered at wavelengths of 450, 550, 830 and 940 nm. On July 7 1998, calibration data was obtained through 550, 650, 750, 830 and 940 nm filters, while on July 9 1998, 450, 550, 650, 750, 830 and 940 nm photometry was obtained.

The 1997 November 22 observations were made at an eastern elongation. Mercury was studied

before and during sunset and observations of the calibration star ϵ Aqr (HR 7950) initiated after Mercury's altitude reached the telescope's hardware limit of 6° , when the altitude of ϵ Aqr was 35° . Skies were photometric and no haze was apparent.

The 1998 observations were also made at eastern elongation with 12 Com (HR 4707) chosen as calibration star on July 7 and 36 Leo (HR 4031) on July 9. The skies were cloud-free but dusty haze was present, especially on the first date. The haze was layered above the observatory altitude which caused the optical depth to vary significantly at high zenith angles.

In the disk-resolved spectrophotometry presented here, observations made on October 22, 1995, are also considered but were excluded from analysis due to a large instrumental chromaticity within the wide filter bandpasses used on this date. This is further discussed in Section 5.1.

Dusty circumstances accentuate the need for calibration star observations to be made temporally close to Mercury observations with a high temporal resolution, through the same sky path and air masses as those traversed by Mercury. Ideally, calibration observations should be performed concurrently with Mercury to minimize calibration errors introduced by variations in atmospheric and dust opacity and sky color with time and solar altitude. Due to the short timespan during which Mercury was observable in good seeing conditions and to limitations in telescope pointing, this was unfortunately not feasible, which negatively affected the photometric calibration at blue wavelengths.

All three spectra of Mercury displayed an increase in slope toward shorter wavelengths due to changes in the color-dependent atmospheric extinction coefficient in the timespan between Mercury and calibration star observations. For the 1997 observations, five hours elapsed from the time of Mercury observations to the completion of calibration observations. On 1998 July 7 the time difference was four hours while on July 9,

two hours. The "best" correction for extinction is achieved for the nights when the atmospheric dust loading is minimal (1997) and the time interval between Mercury and calibration star observations is smallest (July 9, 1998).

Blue wavelength fluxes are more strongly affected by changes in atmospheric conditions because of the increasing scattering coefficient due to aerosol and dust. In combination with high air masses and temporally evolving absorption properties at a time (sunset or sunrise) when these are subjected to the largest temporal evolution gradients, even a slowly varying isotropic extinction is uncorrectable by the Bouguer method employed here. Rufener (1986) discusses the problem of temporally evolving extinction at short to long timescales and the "M and D method" to correct it, should it display isotropic and homogeneous temporal evolution. However, it was not possible to correct the obtained extinction coefficients for this effect as only one calibration star was observed each night.

In order to remove data points affected by varying extinction, the three mercurian spectra were combined and data points suspected to be outliers (all 450 nm points) were removed. A least squares linear fit was calculated from the reddest data points. A data point was removed if the reflectance value deviated from the fitted reflectance by more than the 1σ envelope of the linear fit and the mean error of the data point did not include the value of the fitted reflectance. An average normalized Mercury spectrum was then obtained from the mean of the accepted data values at each wavelength (650, 750, 830 and 940 nm for July 9, 1998; 750, 830 and 940 nm for July 7, 1998; and 830 and 940 nm for November 22, 1997).

Details on the calibration of the Mercury observations using solar analog flux observations and calibration spectra, as well as a description of photometric measurement method, are given in the Appendix.

4. Disk-integrated Mercury spectrum

The resulting multiphotometry of Mercury for the wavelength range 650 to 940 nm is presented in Fig. 1 and Table 1. The spectrum shows a best-fit linear slope,

$$S' = \frac{[A_p(940) - A_p(550)]/A_p(550)}{\lambda_{940} - \lambda_{550}},$$

of $16.87 \pm 0.31\%/1000 \text{ \AA}$ ($1.687 \mu\text{m}^{-1}$), larger than that of most published spectra but the same as that of a 1984 CCD spectrum (Vilas 1985) in the 600–880 nm "continuum" range, $16.9\%/1000 \text{ \AA}$.

The linear slope indicates that the H₂O absorption band near 930 nm has been well corrected for. It is furthermore evident that a putative pyroxene absorption band due to d shell electronic transitions in Fe²⁺, reported by McCord & Clark (1979) between 750 and 950 nm, is not detected for the 830 and 940 nm data points. McCord & Clark reported a maximum band depth at 890 nm of at most 4% for a spectrum obtained on 21 April 1976. The error bar of the present 940 nm photometry allows a maximum depth of the absorption feature of $\sim 4\%$ relative to the continuum.

The Mercury spectrum in Fig. 1 is a simple arithmetic average of the disk-integrated fluxes measured at phase angles of 58.6°, 80.4° and 84.0° (for November 22 1997 and July 7 and 9 1998, respectively). There is no indication of spectral reddening (i.e., an increase of the visual spectral slope with phase angle) as a function of increasing phase angle, which may be explained by the relatively short wavelength and phase angle range covered. A slight phase reddening effect, amounting to an increase of the $U - B$ color index by 23% and an increase of the $B - V$ index by 2% while the phase angle increased from 73° to 110°, was reported by Irvine et al. (1968). This effect was not confirmed in a 410 nm/950 nm color ratio study of published spectrophotometry obtained by various investigators at a similar

(71–120°) range of phase angles, using different instrumentation under varying observing conditions (Blewett et al. 1997a).

The photometric data presented here supports the results obtained from the well-calibrated filter photometer spectrum recorded by Vilas on 5–7 October 1974 (Vilas et al. 1984, Blewett et al. 1997a) which indicates the absence of an absorption feature near 950 nm. Both the 1974 and 1976 spectra have been criticized by Vilas (1985) who suspected slight errors in their calibration. Other published spectra are more severely affected by incomplete removal of telluric absorptions, including the 1984 CCD spectrum (cf. Blewett et al. 1997a).

5. Disk-resolved photometry of albedo features

Images of the Mercury disk subjected to processing by darkframe and flatfield only were used to study possible spectral differences between the subsets of the very brightest and darkest albedo regions. The goal was to determine whether the spectra of bright and dark groups of albedo regions differ in spectral slope with respect to illumination geometry, thus possibly indicating different surface composition and/or maturity. Since multicolor imaging observations were acquired only for the poorly known hemisphere (longitudes 160–340°), a determination of the true geologic identity of the studied albedo features based on spectral characteristics and color information from Mariner 10 data can unfortunately not be made.

5.1. Disk-resolved photometry: Measurement method

For the study of reflectance vs. illumination geometry the integrated disk fluxes were set to the disk-integrated geometric albedo for the proper wavelength. The albedo of the 550 nm images was set to 0.138, determined for λ 554 nm from Earth-based observations (Veverka et

al. 1988). The geometric albedo for 650 nm was determined to 0.160 from the slope of the Vilas (1984) CCD spectrum and the albedo at 550 nm. Longer wavelength albedos were calculated from the 650 nm albedo and the spectral slope determined in this work (Table 1).

Fluxes of individual features were measured with the same aperture sizes for all wavelengths. The flux from a specific feature is thus averaged with that of the surroundings to a degree depending on the effective resolution for the proper wavelength and image. However, since all feature flux measurements were made on the same set of images with seeing approximately constant over the Mercury disk, and since we are interested in the *relative* difference between the equally seeing-affected bright and dark feature spectra, this is of no major consequence for the results. Furthermore, the variation of spectral slope with emission angle for an averaged Mercury regolith, formed by the scattering properties of both bright and dark albedo features, is not affected.

Circular apertures with radii of four pixels were used for the disk-resolved photometry, corresponding to spatial footprints on the central Mercury disk of approximately 190, 260 and 230 km for the 1995, 1997 and 1998 runs, respectively. The aperture size was smaller than the optical resolution of the SVST defined by the passbands for all wavelengths, except for V+W12, 550 nm and 650 nm filters (see Table 2 of Warell & Limaye 2001).

The feature spectra from 1995 October 22 show a flux decrease towards red wavelengths relative to the total disk flux. This is attributable to the fact that the angular resolution decreases as the chromatic aberration within the effective filter bandpasses increases. A larger fraction of the total disk flux is therefore refracted increasingly further from the disk, decreasing the relative flux in sub-disk apertures. A similar effect is seen for 1997 November 22 photometry, which was obtained at worse seeing conditions than the

image data for 1997 November 20 and 1998 July 9. The 1995 and 1997 November 22 data are therefore not further considered in terms of individual feature photometry. The following analysis will thus be limited to the 1997 November 24 and 1998 July 9 data sets, which were obtained at the most stable atmospheric conditions, with identical optical filters and with the most complete spectral coverage.

Flux measurements on the Mercury disk were obtained for emission angles $-53^\circ < e < 65^\circ$ at phase angles of 63.4° (1997) and 84.0° (1998). At a phase angle of 90° , the terminator region has incidence angles approaching 90° while the emission angle is close to zero. The incidence angle decreases towards zero and the emission angle increases towards 90° as the limb is approached. For decreasing phase angles, the bidirectional reflectance distribution on a sphere with constant albedo becomes more uniform (see, e.g., Vilas et al. 1984) and the difference in incidence and emission angles between equally separated points becomes smaller. Effects on the spectrum due to variations in these parameters should thus be expected to be smaller for the 1997 data. It should be remembered that the range of emission angles sampled within the photometric aperture grows towards the limb, while the inverse is true for the incidence angle. Limited angular resolution therefore effectively reduces spectral effects strongly dependent on such geometry.

5.2. Disk-resolved photometry: Results and discussion

The obtained multicolor photometry of bright and dark surface features, identified in Table 2, are shown in Fig. 2 and 3. The spectra are all normalized at 550 nm for improved visualization of any differences in spectral slopes. There is no significant difference in the slopes of averaged bright and dark feature spectra for the wavelength range 550–940 nm for either of the two runs, though the average dark feature displays a marginally redder slope for a phase angle of 84°

(1998 run).

The effect of varying emission angle on the spectral slope is shown in Fig. 4. There is a clear inverse correlation between the spectral slope and emission angle (the "inclination") for bright and dark features, i.e. the spectra become redder as the terminator is approached. The slope increases from $\sim 13\%/1000 \text{ \AA}$ to $\sim 24\%/1000 \text{ \AA}$ from large to small absolute values of emission angle. The relation between spectral slope and emission angle is linear at first approximation and the same within 1σ error bars for both bright and dark features ($(dS'/de)_b = 0.116 \pm 0.032\%/1000\text{\AA}/^\circ$ and $(dS'/de)_d = 0.118 \pm 0.041\%/1000\text{\AA}/^\circ$, respectively).

The magnitudes of mercurian spectral slopes may be compared with those of lunar anorthosite regions which have rather linear spectra and as such are possible analogues to the Mercurian regolith. A number of spectra of fresh and submature lunar anorthosite regions are discussed by Blewett et al. (1997a). These have spectral slopes in the range 3–6 %/1000 \AA , which is a factor 3–5 smaller than the disk-resolved spectra obtained here. Spectra of mature lunar anorthosite regions have not been obtained but such regions should have larger slopes due to a higher degree of maturity (Rava & Hapke 1987, Hapke 2001).

A direct comparison of the mercurian and lunar spectral slope–emission angle relations is possible from laboratory bidirectional reflectance measurements of returned lunar soils. Pieters et al. (1991) measured the spectral reflectance from 350 to 2500 nm for four soils of different maturity and composition at a range of phase and emission angles. Spectra of bulk surface soils from highland stations (Apollo 14 #14259.150, mature and developed on breccias; Apollo 16 #62231.140, mature) and mare stations (Apollo 11 #10084.255, mature; Apollo 12 #12070.853, submature) were sampled at the bandpasses of the photometry conducted here, and mean spectral slopes for phase angles $60\text{--}100^\circ$ and emission angles $0\text{--}60^\circ$ were calculated (see Fig. 4). The

spectral range 550–750 nm was sampled (shortward of the ferrous absorption) to obtain the slope of the "continuum" of the spectrum, which is the spectral parameter that is measured for Mercury.

Typical regolith spectral slopes for submature and mature maria and mature highlands fall in the same range, 13–20%/1000 Å. All lunar spectra display the same general increase in slope with decreasing emission angle as the mercurian regolith, but the inclination is considerably smaller. The mature Apollo 14 soil provide the best fit to the mercurian spectrum both in terms of magnitude of the spectral slope and the inclination of the spectral slope–emission angle relation, but the submature Apollo 12 sample fit is very similar. Slopes of lunar spectra redden significantly more for NIR wavelengths than for visual wavelengths as the phase angle is increased, and all lunar soils measured show strong backscattering properties over the range of emission angles measured for Mercury (Pieters et al. 1991). The fact that both the inclination of the slope–emission angle relation and the increase of albedo towards longer wavelengths is larger for Mercury indicates that the backscattering of its regolith is stronger for longer wavelengths than is the case for the Moon.

The present spectrophotometry shows that it is not possible to detect any spectral differences between bright and dark features at a spatial resolution of 200–300 km. Of specific interest is the fact that the bright features, of which ~70% are ray craters (Warell & Limaye 2001), do not exhibit bluer spectra than dark features. Ray craters were observed to be ~12% brighter than surrounding smooth or intercrater plains, in 355 nm/578 nm color ratio images obtained by Mariner 10 (Hapke et al. 1975). These wavelengths are outside the range for high-resolution SVST image data. However, if the blue spectral slope is caused by ilmenite, the relative color difference should persist into the NIR (Rava & Hapke 1987). This is also the quantitative effect

of increased maturation in a lunar-like regolith due to the presence of sub-microscopic reduced iron in soil grains and agglutinates (e.g., Hapke 2001). There is a possible bluening of bright features relative to dark for the longest wavelengths of the average spectra (750–940 nm, Fig. 2 and 3), but this effect is not statistically significant.

Probable explanations for this apparent discordancy is that either bright feature spectra are significantly mixed (intimately or areally at spatial resolutions much smaller than ~300 km) with more mature (redder, darker) feature spectra presumed to compose the underlying strata, or that the large spatial size of the photometric apertures combined with inadequate resolution prevents effective separation of the spectra of the two feature types if they are areally mixed at resolutions of the order of 300 km. It may also be speculated that ilmenite is not the major neutrally opaque phase present as fresh (bright) feature spectra should then display the 1-micron ferrous absorption feature; however, very few if any fresh craters are probably as large as 300 km and any ilmenite present would therefore not contribute significantly to the reflected flux within the apertures used.

The possibility that spectra within the individual groups of dark and bright albedo features are dissimilar due to different geologic natures cannot be studied at present as photometric disk-resolved observations have not yet been performed of the well-known hemisphere for which geologic information is available. The errors introduced by the assumption that all features within one group are spectrally identical are therefore not known. Robinson & Lucey (1997), based on recalibrated Mariner 10 imaging data, showed that albedo is not a definitive diagnostic indicator of composition or compositional differences of the regolith, while color ratio is. There is no indication that this should not be true also for the poorly known hemisphere (as for the areal distribution of bright albedo features, the two hemispheres are identical at 200 km resolution

(Warell & Limaye 2001)). Therefore, it is not unexpected that the two groups of features have on average similar spectra. To resolve this issue, higher-resolution image data is clearly necessary to extract spectra and color ratios from smaller surface regions.

6. Spatial variation of ferrous band strength

In order to evaluate the existence of spatial variations in the strength of the plausible 1-micron ferrous band absorption across the disk of Mercury, images obtained in the 940 nm band were ratioed to continuum band images. Images were used for which no removal of the light scattering function (photometric normalization) had been done. This was made to avoid error introduced by effects of the photometric fitting procedure, limited resolution and atmospheric seeing. In the following, it is assumed that the photometric function is independent of wavelength for the range of incidence and emission angles present on the mercurian disk. The analysis furthermore shows that any such differences are smaller than the noise in the data for the photometric geometries and wavelength range considered, as no regional-scale gradients in the produced color ratio maps are visible.

6.1. Ratio image analysis method

Ratio images were calculated from the highest resolution darkframe-subtracted and flatfielded image data available. The mean sky level outside the region affected by scattered light from the Mercury disk was set to zero after which the total disk flux was set to the spectral reflectance value for the proper wavelength band (Table 1). The images were aligned and cropped with respect to the illumination center of the disks. Alignment of the two images contributing to the ratio image was made by fitting two-dimensional Gaussian profiles to the disks and obtaining the illumination center coordinates. The accuracy

of the relative alignment was checked by cross-correlation which was found to produce the same best-fit coordinates but with a significantly increased computational time. The denominator of the two input images was subsequently rotated to conform to the rotation angle of the numerator image, and the ratio computed. A ratio image computed from images obtained with the same filter at the same angular resolution should ideally be perfectly "flat", i.e., it would have a mean pixel intensity of one and an intensity variance of zero. The "flatness" was evaluated in terms of the variance of the pixel intensities centrally on the Mercury disk. While input images of similar resolution were selected, a small amount of smoothing of the sharpest (shorter wavelength) image would generally provide a smaller value for the variance.

The magnitude of intensity variance for different degrees of smoothing was studied by treating the (sharper) denominator image with two-dimensional Gaussian and running-average boxcar filters, followed by ratioing. Gaussian filter sizes ranged from 5 to 41 pixels with Gaussian widths of 2 to 20 pixels, boxcar filter sizes were 2 to 20 pixels. The Gaussian filter was applied to approximate the perfect PSF profile of a point source, while the rectangular profile of the boxcar filter chosen as it better approximates the PSF of a stellar source affected by scintillation noise.

The image restoration procedure is difficult to perform with good results since the effects of spatially varying seeing on scales smaller than the disk size forces the use of an adaptive filter to obtain a uniform angular resolution. The size, shape and intensity of an adaptive filter is an unknown function of image coordinates as the PSF at each coordinate and time cannot be determined. The magnitude of the angular and temporal effects of seeing for the SVST Mercury observations may be easily estimated. Given a median Fried parameter of $r_0 = 12.4$ cm at La Palma (Scharmer 1998), an assumed vertical distance to the effective seeing layer of 5000 m and

an airmass of 5, the isoplanatic angle is of the order of $\Theta_0 \sim 0.32''$ which is only a few per cent of Mercury's typical disk size. For the best seeing conditions experienced 5–10% of the time, equivalent to $r_0 > 20$ cm, Θ_0 increases to $\sim 0.52''$ or larger. Given an average speed of turbulence of 10 m/s, the time scale of temporal variations across the wavefront are $\tau_0 \sim 4$ ms, resulting in a typical seeing image motion timescale of ~ 16 ms for the SVST. As the Mercury disk size is approximately an order of magnitude larger than the isoplanatic patch and the exposure times used for imaging Mercury were at least twice and generally an order of magnitude longer than the seeing image motion timescale, the seeing distortion was usually severe (an appreciation of this comes from the fact that typically only about 0.5% of the Mercury images recorded by the SVST qualified for further analysis). The approach of using spatial filters whose properties are constant in the image plane is thus in theory insufficient, but may be a good approximation of the properties of an average temporally and spatially smearing filter. Observations of photometric calibration stars at several runs showed that their shapes at the short exposure times involved were, due to scintillation, most frequently approximated by flat square-shaped profiles with dimensions several factors larger than the resolution limit at the filter wavelength. Only rarely was a PSF observed that approached that of a symmetrically blurred perfect point source with a significantly brighter center and symmetric halo.

From each ratio image, filtered with boxcar or Gaussian filters of varying sizes, a relative intensity image R was formed. The pixels of the ratio image were binned to form effective (merged) pixels from $s \times s$ original pixels ($s = 1, 3, 5, 7, 9$) having intensities equal to the average of the contributing pixels. From the intensity of each binned pixel $I_{x,y,s}$ and the average value of its four-neighbors, $\langle I_{C,s} \rangle$, the pixel intensities in the R map are formed from

$$R_{x,y,s} = 100 \frac{I_{x,y,s} - \langle I_{C,s} \rangle}{I_{x,y,s}}$$

where

$$\langle I_{C,s} \rangle = \frac{1}{4} (I_{x+1,y+1,s} + I_{x-1,y+1,s} + I_{x+1,y-1,s} + I_{x-1,y-1,s}).$$

The relative intensity image R is thus effectively a small-scale gradient map, enhancing pixels whose intensities, at the scale of the binned pixel size s , are deviating from the surroundings.

The flatness of the R map, i.e. the intensity variance of the central disk pixels of the ratio image, was evaluated by the standard deviation σ of the pixel intensities. To evaluate the statistical significance of the intensity variations of the R map pixels, the number of standard deviations that each disk pixel differed from the average disk value was calculated. A disk variation map V was thus formed according to

$$V_{x,y,s} = \frac{R_{x,y,s} - \langle I_{\text{disk}} \rangle}{\sigma_{\text{disk}}}$$

where $\langle I_{\text{disk}} \rangle$ is the average intensity of central disk pixels and σ_{disk} the corresponding standard deviation. R and V maps were calculated for a number of values of s since the input images were well oversampled with respect to the resolution of the original ratio images (Warell & Limaye 2001). A barely resolved feature with a spatial size equal to the resolution limit therefore has a characteristic size of several pixels. The value $|V_{x,y,s}|$ is larger the more deviating the pixel intensity is from the surrounding mean, and is maximum for the binned pixel size s best matching the spatial size of the feature. The $V_{x,y,5}$ map was used to evaluate the statistical significance of ratio image variations. For this choice of s , the binned pixel size was not too small to severely limit the spatial information, while still sufficiently large not to significantly reduce S/N .

The actual detectability limit for a disk feature in the ratio images is determined by a number of factors, including the pixel noise, the feature location with respect to binned pixel centers, and seeing distortion. The S/N ratio for disk pixels ranged from ~ 25 for 450/450 nm images to ~ 60 for 830/830 nm images. For 940/continuum images the S/N ratio was $\sim 32 - 53$. As discussed above, the seeing is slightly spatially varying across the disk of Mercury even for the highest resolution images, thereby affecting the disk shape and the location and intensity of disk features. A frame of reference to assess the statistical significance of disk pixel variations thus has to be established to draw conclusions on the existence or non-existence of physical color variations on Mercury's surface.

6.2. Ratio image analysis

To assess the influence of seeing distortion on the intensity variations on the disk, $R_{x,y,5}$ and $V_{x,y,5}$ maps were calculated for the *individual images* contributing to the ratio images. The majority of disk pixel intensities of the R map varied by less than 1% from the mean. At the bright limb the variation was greatest with deviations of 4–5%, resulting from the significant intensity gradient. For the V map, a 5×5 pixel box centrally located on the disk of Mercury was used to obtain an estimate of the variance of the disk intensity values. A very small number of disk pixels (0–3 of ~ 70) showed standard deviations of $> 2\sigma$ or more on the V map, while pixels at the limb invariably showed variations at least this large. For the majority of pixels deviant by $> 1 - 2\sigma$, V maps obtained from similarly resolved images and with identical optical filters are consistent in terms of pixel location and intensity due to the spatial distribution of albedo features. V map variations are also consistent for images obtained with different filters.

A ratio image obtained from identically resolved *same-filter* images should be flat within the noise level. The sky pixel intensities will show

a very large standard deviation as they are the quotient of very small numbers, but for a sufficiently large number of sampled sky pixels their average value is unity. The mean level for the R and V maps is then zero for a sufficiently large disk pixel sample, and the disk is featureless. Ratio images based on a numerator image of poorer resolution than the denominator image will result in a ratio image with bright disk edges and disk detail.

For a similar study of *continuum-filter* ratio images, the total flux of the Mercury disk was set to the spectral reflectance value for the proper wavelength band (Table 1) prior to ratioing. The variation of image scale relative to a minimum of telescope back focal length occurring near 550 nm was ignored as it varied by a maximum of only 0.3% for the 550/940 nm ratio.

Based on this analysis it is safe to state that, should scattered disk pixels show variations of $< 2\sigma$ on the continuum/940 nm V maps, these are not uniquely attributable to ferrous band strength variations in the mercurian regolith. It is additionally required that pixels deviant by 2σ or more are consistent in location and number on at least a majority of continuum/940 nm maps in order not to be regarded as spurious artifacts.

For 1997 November 22 observations, two *ferrous band to continuum* (940 nm/550 nm) ratio images were produced from two different sets of input images. On-disk pixels were $\leq 1\sigma$ deviant, except for two scattered dark pixels on one V map which were $\geq 2\sigma$ deviant. No consistent pattern of deviant pixels are visible in the ratio images. R map differences were $< 2\%$. The result is illustrated in Figure 5. From the 1998 July 9 run, twelve images were used to produce two each of 940/550, 940/650 and 940/830 nm ratio images. Again, results were similar. Typical maps are shown in Figure 6.

The conclusion is that no variation in 1-micron ferrous band strength is detectable on the Mercury disk for either the 1997 longitudes ($\sim 170 - 240^\circ$) or 1998 longitudes ($\sim 240 - 290^\circ$). These

locations are almost entirely on the hemisphere not imaged by Mariner 10.

7. Regolith maturity and FeO content from the Mercury spectrum

A relationship between soil maturity and iron content of lunar-like materials was predicted by Hapke (Hapke et al. 1975, Rava & Hapke 1987) and was observationally confirmed for the Moon by Lucey et al. (1995). The position of a lunar soil in the parameter space defined by the ratio of bidirectional reflectances at 950 nm and 750 nm, and the reflectance at 750 nm, is a function of soil iron content and maturity. Blewett et al. (1997a) applied the relationship to Mercury, assuming that the behaviour of mercurian spectra conforms to the assumptions of the Hapke model, i.e. the general UV-NIR reflectance properties of a mafic silicate regolith are determined by ferrous iron (Fe^{2+}) in constituent minerals, by fine-grained metallic iron (Fe^0) produced by maturation, and by spectrally neutral opaque mineral content.

For the Mercury spectrum of the poorly known hemisphere reported in this work, the relation established for the Moon by Lucey et al. (1995) places it in the group of Mercury spectra from which a negative ferrous iron content was inferred by Blewett et al. (1997a). Specifically, the abundance of FeO in the regolith is found to be -8.8 ± 6.6 wt%. While this points to a mercurian regolith low in FeO and mature with respect to lunar highland soil (from the 750 nm albedo), it may also indicate that the photometric reduction may be in error (due to, e.g., a varying extinction coefficient), or that the lunar maturity-iron relation does not hold for Mercury. The photometric reduction performed here is considered to be robust, while the validity of the lunar maturity-iron relation for Mercury is still an open issue.

Blewett et al. (1997a) determined a range of -14.7 to 9.5 wt% FeO content of the mercurian regolith from published spectra and interpreted

those giving negative iron content as due to low FeO and incomplete correction for atmospheric water band absorption. Another explanation for erroneous values and their generally large scatter may be that very few, if any, published spectra of Mercury are properly reduced with respect to telluric absorptions and solar or calibration star spectra. This is not unlikely given high air masses frequently encountered during observations and long time delays between Mercury and calibration observations. This conclusion is supported by the lack of any detectable integrated disk phase reddening of Mercury for the phase angle range $71\text{--}120^\circ$ (Blewett et al. 1997a), though such a dependence is clearly observed for the integrated Moon (Lane & Irvine 1972; for the V-band, the lunar phase curve was shown to fall off by 16% for the same phase angle range), returned lunar soil samples (Pieters et al. 1991) and the Mercury photometry by Irvine et al. (1968).

8. Discussion and conclusions

The published vis-NIR spectra of the integrated Mercury disk are discussed by Blewett et al. (1997a) in relation to the current knowledge of the spectral properties and composition of the Moon. Several lines of evidence point to a very mature regolith similar in composition and scattering properties to, though more mature than, the lunar highlands. The spectral slope is similar to that of lunar anorthosite-rich (high-Ca plagioclase feldspar) regions. The lack of significant absorption features in the vis-NIR spectrum is due to vapor deposited coatings on soil grain surfaces and in agglutinates containing sub-microscopic metallic iron particles generated by meteorite impacts and solar wind sputtering. Their effect is to lower the spectral contrast and redden and darken the spectrum (Hapke 2001). The ratio of geometric albedos at 950 and 750 nm to the albedo at 750 nm has been used to infer a very mature regolith with a low FeO content of ~ 3 wt%, based on the lunar calibration by Lucey

et al. (1995). A low TiO_2 content is compatible with the high normal albedos and blue colors of mercurian crater rays. A regolith composition corresponding to approximately <1 wt% TiO_2 in ilmenite has been inferred from a lunar calibration (Blewett et al. 1997b, Lucey et al. 1998) and is consistent with microwave opacity measurements (Jeanloz et al. 1995).

The shortage of detailed information on the mercurian regolith composition is to a substantial part due to the difficult conditions encountered by ground-based observations. These are discussed at some length by Mendillo et al. (2001). Ground-based imaging of Mercury has been unable to reach the necessary angular resolution to study spatial variations of possible spectral absorption and emission features on the Mercury disk, which could provide information on mineralogically homogeneous regimes of the surface and geological provinces on the hemisphere not imaged by Mariner 10.

The integrated Mercury spectrum presented in this work (Fig. 1) has a homogeneous linear slope about twice as large as the majority of published spectrophotometry. The slope is identical to that of the most recently published spectrum, obtained with a CCD camera (Vilas 1985). The lack of absorption in the 940 nm passband indicates that the correction for telluric water absorption is good and that the depth of any ferrous absorption band is less than 4% relative to the continuum.

The vis-NIR spectral slopes of albedo features on Mercury are shown to be strongly inversely correlated with emission angle, i.e. the spectrum reddens as the terminator is approached (Fig. 4). This relation is considerably more inclined than the lunar (as obtained from laboratory measurements) for the same phase angle. If there indeed is only a marginal phase reddening effect for Mercury (i.e., the effective scattering particles have a largely isotropic phase function) as indicated by Blewett et al. (1997a), this behaviour is a consequence mainly of a wavelength-dependent

angular scattering function of the particles. The higher geometric albedo for Mercury compared to the Moon at long wavelengths and the greater inclination of the spectral slope-emission angle relation, is consistent with the typical effective scattering particle being more strongly backscattering than what is observed for the lunar highlands, and that the backscattering is more effective for longer wavelengths.

This conclusion is supported by microwave opacity measurements which show that the effective specific loss tangent of Mercury's regolith is at least 2 and 1.4 times smaller than that of the lunar maria and highlands, respectively, and approximately this smaller than typical terrestrial basalts (Mitchell & de Pater 1994). This indicates that the radar beam impinging Mercury's surface suffers less scattering losses in the material, increasing the probability of backscattering, and that its regolith is considerably more transparent than the lunar at wavelengths from 0.3 to 6 cm. The effect may be due to mineralogical differences between the surfaces of Mercury and the Moon; specifically, refractory Ti- and Fe-bearing rock forming minerals, characterized by high microwave opacities, should be significantly less abundant in the mercurian crust (Jeanloz et al. 1995). The striking correlation between increasing wavelength and decreasing specific loss tangent (thus increasing backscattering efficiency) found by Mitchell & de Pater (1994), as well as the significantly higher optical transparency of Mercury's top-soil compared to the Moon's, is demonstrated to be continuing into the vis-NIR spectral range in this work.

Starukhina (2001) finds from a study of dielectric loss measurements of silicates, Mercury and the Moon that cold silicates may readily explain the radar backscattering signals found on those planets. Particularly, an extremely low temperature is neither a necessary nor a sufficient condition for low dielectric loss and high radar brightness, and may be explained by differences in silicate material properties (activation energy)

between surface regions. Starukhina (2001) also points out that the considerably larger (a factor of ~ 2.5) circular polarization ratios for polar craters of Mercury compared to the value for the lunar poles, as well as the lack of radar-bright polar craters on the Moon, is consistent with a difference in surface composition between the two bodies as the temperature within permanently shaded craters are expected to be similar. The non-necessity of water being responsible for the backscattering property of the mercurian regolith is fully consistent with the findings in this paper, since the spectral slope–emission angle dependence is of the same order of magnitude for albedo features from all measured latitudes and both (bright and dark) feature types, indicating that silicates are globally distributed. The observation that the lunar and mercurian mineralogies seem to be significantly different in the sense of the circular polarization ratios is supported by the large difference in inclination of the slope–emission angle relation with that of the lunar seemingly being much smaller, consistent with a smaller surface backscattering efficiency. The relations are also consistent with lower dielectric losses being more probable for optically bright materials with lower static permittivity (Starukhina 2001), as Mercury’s visual physical albedo is 0.14 compared to 0.11 for the Moon (Veverka et al. 1988).

The close similarity in location of extreme (very bright and very dark) mercurian albedo features in the spectral slope–emission angle diagram compared to the situation for mare and highland lunar soils measured in the laboratory indicates that the regolith is considerably more homogeneous in its light scattering properties than that of the Moon, i.e. that the maturity difference between geologic provinces (smooth plains, intercrater plains and ray craters) is relatively smaller, and that there is no well-defined relation between reflectance and mineralogical composition. This supports the conclusions of Rava & Hapke (1987) that the mercurian regolith

is chemically more homogeneous and of Robinson & Lucey (1997) that albedo is not a definitive diagnostic indicator of composition, both based on color ratio images from Mariner 10.

Laboratory measurements of some plausible mercurian end-member minerals have been performed to investigate spectral slope variations with phase and emission angle, and give an indication of possible spectral evolution with respect to phase and emission angles. Gradie et al. (1980) concluded that variations in geometry mainly affects the shapes of spectral reflectance curves. They present normalized reflectance spectra of powdered basalt (normal reflectance 0.22 in the visible, grain size 45–75 μm) at a phase angle of 60° . For the wavelength range 550–940 nm, the effect of increasing the emission angle from 0° to 60° is to increase the spectral slope from ~ 5.1 to $\sim 5.6\%/1000 \text{ \AA}$. Spectral evolution for the pure pyroxene hedenbergite (normal reflectance 0.25 in the visible, grain size 75–150 μm) which has prominent absorption bands at 700 and 900 nm, causes the contrast of the absorption bands to first increase, then decrease, when increasing the emission angle from 0 to 60° at a phase angle of 60° . The spectrum is blue in the wavelength range 550–940 nm with a slope of $-3.1\%/1000 \text{ \AA}$ calculated at the above extreme wavelengths, at which the relative reflectances also varies the least in the considered wavelength range between the two extreme emission angles. The spectral slopes and variations with emission angle exhibited by these two materials are considerably smaller than those measured for Mercury. If the mercurian regolith consists of significant amounts of these minerals, they must be very mature and mixed with opaque phases or ferric iron in order to reduce the total reflectance, significantly redden the spectrum and decrease the contrast of absorption features.

Pieters et al. (1983) studied the effect of varying phase angle on a particulate sample of pure enstatite orthopyroxene (EN_{89}) at phase angles of 60° and 90° . The overall bidirectional re-

flectance decreases with phase angle and the contrast of the 910 nm absorption band decreases by about 6%, causing the spectrum to redden. The effect of arithmetic averaging of higher with lower phase angle spectra is thus to increase the possibility of detecting a pyroxene band due to Fe^{2+} charge-transfer absorption in agglutinitic glasses, as noted by Vilas (1985). Mustard & Pieters (1989) studied the bidirectional reflectance of particulate olivine of grain size range 45–75 μm for a range of geometries. For a constant phase angle of 75° and increasing incidence and emission angles from $i = 15^\circ, e = -60^\circ$ to $i = 60^\circ, e = -15^\circ$ a spectral bluening by 4% is observed in the wavelength range 600–950 nm as the contrast of the wide 1-micron absorption feature increases. For a mercurian regolith areally mixed with enstatite pyroxene and olivine with the above grain sizes their effects on the vis–NIR spectrum due to photometric geometry may therefore largely cancel (not considering the contrast lowering effects of opaques or agglutinates which would facilitate such effects).

A color ratio image analysis (Section 6) shows that the spatial variations in the strength of any ferrous band absorption is $<2\%$ relative to surrounding regions at spatial scales of 200–300 km on the poorly known hemisphere, and that the shape of the photometric phase function is apparently non-varying within the covered wavelength range. The non-detection of color variations in continuum-ratio and ferrous band/continuum images presented here is consistent with the Mariner 10 color ratio map (Robinson & Lucey 1997), where significant differences between geologic units occur at scales smaller than 200 km. The result is also consistent with the mid-infrared imaging study of Sprague et al. (2000) who were not able to detect any spatial flux variations exceeding 5% on color ratio images in the 8.1–12.5 μm spectral range. They attributed this to poor angular resolution (though nearly diffraction limited resolution was obtained for long wavelengths), large pixel size and small

disk diameter of Mercury. That study also utilized flux-calibrated multispectral imaging data of the integral disk to infer a regolith composition indicative of the Mg-rich pyroxene bronzite, the ultramafic rock picrite and the tectosilicate sodalite. Cooper et al. (2001) presented comparatively featureless mid-infrared emissivity spectra of Mercury for a range of longitudes and concluded, based on locations of transparency features, that they indicated the presence of intermediate, mafic and ultramafic rock types. However, the considerable variations in the general shapes of published infrared emissivity spectra of Mercury, the small amplitudes of spectral features and the differences with respect to silicate minerals suggest that additional observational work would help clarify the situation.

Application of the iron–maturity versus opaque mineral calibration for the Moon (Lucey et al. 1995) to the integrated Mercury spectrum presented here indicates a mature regolith but provides negative values for the FeO content, as is the case for the majority of published spectrophotometry (Blewett et al. 1997a). All but two or three published spectra of Mercury, all disk-integrated, give inconsistent abundances when the lunar FeO and TiO_2 calibrations are applied to Mercury (Blewett et al. 1997a). Poorly calibrated spectra are presumably caused by contamination by telluric lines, bad choices of solar analogs or calibration stars, varying atmospheric extinction, etc. In as much as the mercurian regolith is assumed to be very lunar-like, it is therefore of interest that not even the highest-quality spectra of Mercury display the characteristic lunar-like disk-integrated phase reddening effect. A mercurian regolith that is more mature (Cintala 1992) and chemically more homogeneous (Rava & Hapke 1987) than the Moon’s would exhibit a stronger phase reddening since slope increases with maturity (Pieters 1993) and the slopes of lunar soils increase with phase angle (Lane & Irvine 1972). This indicates that even the “best” spectra of Mercury may be poorly cal-

ibrated, and that conclusions based on lunar calibrations will not be correct.

It is not straightforward to compare disk resolved remotely sensed vis-NIR spectra of the Moon to those of Mercury, for two main reasons. Firstly, for a given feature, a range of spectra for varying emission angles at a given phase angle cannot be obtained for any of the bodies from an Earth-based perspective. Secondly, the lunar surface displays considerable compositional heterogeneity compared to Mercury, which specifically for the Moon necessitates study of a carefully selected region throughout the phase and emission angles of interest. For Mercury, current remote sensing and analysis techniques are not able to register compositional variations as shown in this paper, allowing its regolith in this respect to be assumed as compositionally homogeneous.

Considering measurements of prepared laboratory samples of returned lunar soils, these are close representations of the true lunar regolith in terms of particle size and size distribution, but not in terms of properties of the surrounding medium (vacuum, temperature, electromagnetic environment), soil porosity, macroscopic surface roughness and shadow-hiding effects. The characteristic spatial scale of the latter two parameters are of the order of millimeters in the laboratory, rather than millimeter to centimeter and larger scales for the actual lunar surface. This problem has been discussed by Shkuratov et al. (1999a) who concluded that the brightness phase functions of laboratory and natural regoliths should be significantly different. In lack of sufficient spectral data for the true lunar surface, comparison of the remotely sensed Mercury multicolor photometry obtained here has necessarily been made to laboratory lunar soil measurements.

Much of the present knowledge of the regolith of Mercury is based on comparison with lunar remote-sensing data calibrated with "ground-truth" returned lunar samples. Several impor-

tant lines of work have to be followed in order to understand the remotely sensed spectra of Mercury using this approach. In the laboratory, a study of the spectral evolution of a typical lunar anorthosite in vacuum conditions with respect to geometry, elevated temperatures, grain size and mixed-in opaque phases and ferrous iron would be of interest, since this is a favoured composition of the mercurian regolith. Observationally, disk-resolved imaging spectroscopy or low-dispersion spectroscopy with spatial resolution over a very wide range of phase angles is needed to understand the spectral effects of viewing geometry of the planet's regolith itself. This would provide an improved comparative database to use in conjunction with modelling and laboratory measurements. Such studies would provide constraints on the regolith microscale properties, the surface mineralogy and its spatial and abundance variations, as well as the distribution of archetypical geologic units on the poorly known hemisphere. A well-developed photometric theory such as that of Hapke (1993) and Shkuratov et al. (1999b), including the recent understanding and modelling of regolith maturation as an effect of solar-wind production of sub-microscopic ferric iron (e.g. Hapke 2001, Starukhina & Shkuratov 2001), should be applied to the Mercury spectrum and spectral slope-emission angle relation found in this work to provide further information on the regolith properties of Mercury.

Acknowledgements

This work has been performed within the framework of INTAS grant 99-403, provided by the European Union and the European Space Agency. Göran Scharmer and the SVST staff are much thanked for providing generous access to the telescope facility. The Swedish Vacuum Solar Telescope is operated on the island of La Palma by the Royal Swedish Academy of Sciences in the Spanish Observatorio del Roque de los Muchachos of the Instituto de Astrofísica

de Canarias. Carlé Pieters generously provided laboratory reflectance spectra of lunar samples. David Blewett and another, anonymous, reviewer are thanked for their valuable comments which improved the manuscript.

Appendix: Details on the data calibration procedure

Calibration star photometry

On all dates, the standard stars were acquired and observed in focus immediately following the Mercury imaging sequence. The stars were selected according to brightness, declination (in order for the star to pass through the same range of altitudes and azimuths as Mercury, the declinations should be identical) and right ascension (the star should be located at <1.5 h of RA from Mercury to be able to acquire and follow it through, minimally, the same range of air mass of Mercury as temporally close as possible). In practice, this scheme resulted in three to four completed cycles of calibration observations through the appropriate filters, before the decreasing altitude of the standard reached the mechanical pointing limit of the telescope.

The aperture radius of poor (i.e., subjected to a large degree of scintillation) standard star images were determined by growth-curve analysis. A radius of 3.5 times the FWHM of the major axis of a Gaussian fit to the stellar flux distribution contained all the flux.

To compute the extra-atmospheric (zero air mass) standard star fluxes, the measured magnitudes in each filter were normalized to an exposure time of one second. The background sky flux measured from four surrounding, symmetrically placed, apertures was then removed. A linear least squares fit of magnitude versus air mass was calculated to obtain the extra-atmospheric instrumental magnitude. Following a first fit using all measurements, magnitudes deviating by more than one standard deviation from the mean fitted magnitude for the same air mass were re-

moved. The fit was then recalculated to obtain the reduced instrumental magnitude of the star.

The goodness of the fit was estimated by weighting the observed fluxes with factors equaling the square root of the air mass, the air mass and the squared air mass. Also a scintillation noise weighting was studied (air mass^{3.5}, the power taken to represent an observing azimuth intermediate to the wind direction and at right angles to it) as suggested by some authors for low air masses (e.g., Sterken & Manfroid 1992). For unweighted and air mass-weighted data the photometric fits were good and the obtained zero air mass magnitudes consistent, while the fits were very poor when weighting with air masses to the second power and higher. Unweighted magnitudes were therefore used to calculate extra-atmospheric magnitudes and errors.

Mercury photometry

Aperture photometry of Mercury was performed with circular apertures on images corrected with darkframe and flatfield. The radii of the apertures were sufficiently large to include all the scattered flux from the disk and were determined by growth-curve analysis on poor seeing (i.e. large Mercury disk size) images. It was found that an aperture radius twice the size of the major axis of the disk contained all the disk flux.

Typical S/N (signal-to-noise) ratios for Mercury ranged from 6000 to 9000, while for the standard stars the range was 150 to 800. The theoretically attainable accuracy in the photometry is thus high (errors $<1\%$ or 0.01 magnitude). However, this accuracy is degraded by atmospheric scintillation. Variations in the observed stellar flux for quasi-identical air masses were of the order of 5–15% for all wavelength bands. Scintillation thus contributed to the major error in the measured flux, resulting in a extra-atmospheric errors of typically 0.05 magnitude.

The normalized zero air mass instrumental fluxes for Mercury were calculated by applying the obtained atmospheric extinction coefficients for each filter to the observed Mercury fluxes, using the same data acceptance procedure and no data weighting. Flux variations for quasi-simultaneous observations were of the same order as those observed for the standard stars.

Calibration star spectra

Absolutely calibrated flux spectra for the photometric calibration stars covering the visible to near-infrared wavelength range were constructed by combining data from various sources and were used to calculate normalized fluxes for the Ealing filter passbands.

For the UBVRI standard star ϵ Aqr (HR7950, spectral class A1V), a spectrum for the wavelength range 3225–10525 Å was constructed from Kharitonov et al. (1988) data for 3225–7575 Å with a resolution of 50 Å, and from Glushneva et al. (1998) data covering the range 5975–10825 Å with the same step sequence. The average accuracy is 3.5% for the first data set and better than so for the second (Glushneva, personal communication). These spectra were concatenated at 6325 Å; the Kharitonov et al. (1988) spectrum was used for the shorter wavelengths and the Glushneva et al. (1998) data for the longer wavelengths.

The spectral class of the UBVRI+*uvby* standard 12 Com varies according to the source as F2 (Astronomical Data Center), G5III+A5 (Astronomical Almanac 2000) and G0III-IV+A3V (Kharitonov et al. 1988). The spectrum used for this star was that of Kharitonov et al. (1988) for the range 3225–7525 Å at a data spacing of 50 Å. No measured spectrum for 12 Com could be identified for longer wavelengths. The wavelength range up to 10620 Å was therefore completed with a flux calibrated spectrum obtained from Pickles (1998). From this data set, spectra of an average F2V star as well as combination of average G5III+A5V stars were compared

with the Kharitonov et al. (1988) spectrum for the common wavelength range λ 5000 – 7525 Å. The flux level of the measured 12 Com spectrum and the two average stellar spectra were adjusted individually until a merit function was minimized. The merit function was smallest for the F2V spectrum, for which the mean deviation was 1.8% in the common wavelength range. The G5III+A5V spectrum displayed a very good fit for $\lambda < 7000$ Å where the difference subsequently increased; at λ 7525 Å the deviation was 7%. The average F2V stellar spectrum from Pickles (1998) was thus chosen to represent the flux of 12 Com for $\lambda > 7525$ Å.

The spectrum of the UBVRI+*uvby* standard 36 Leo (HR 4031, spectral class F0III) was obtained from Glushneva et al. (1992). The spectral range of this data set is 3225–10825 Å at a spacing of 50 Å. The mean error of the spectrum is stated as 3.5% for the range 3225–7600 Å.

Solar spectrum

Two solar spectra were used to remove the spectral contribution of the Sun from the Mercury spectra, to provide a check on the calibration errors introduced.

The first solar spectrum used is the flux calibrated spectrum of Neckel & Labs (1984). This data set is given at 10 Å intervals for the wavelength range 3305–6295 Å and at 20 Å spacing for 6310–8690 Å. Extremely weak telluric line absorption is ignored for wavelengths < 5400 Å, which is within the FWHM range of the 450 nm and partly the 550 nm filters. In the range 5400–6860 Å, they corrected telluric line absorption in a non-thorough fashion, and estimate that the errors introduced are $< 0.5\%$ except for a few strong telluric bands. This range is observed by the 550 nm and 650 nm filters. For wavelengths beyond 6860 Å no telluric line correction was applied since such data was then unavailable. Telluric line correction was applied from a study of Kitt Peak FTS spectra; however, an estimate of the error arising from this procedure is not given.

For the range 8725–12475 Å, reliable solar line blocking data was unavailable and flux data is for the continuous spectrum at 50 Å sampling density; errors due to neglecting solar absorption are estimated to seldom exceed 1%. This region falls within the range of the 940 nm filter; the error quoted should also form a usable upper estimate for the wavelength ranges sampled by the 750 and 830 nm filters.

A check on the errors in the Neckel & Labs (1984) solar flux spectrum was provided by constructing a calibrated solar spectrum from observed solar analog spectra and theoretical solar spectra. For the short-wavelength range of this spectrum, 4025–7175 Å, flux calibrated data for 16 Cyg B from Kharitonov et al. (1988) was used. 16 Cyg B has been determined to differ spectrally from the Sun by less than 1–2% at each wavelength at this resolution (Neckel 1986). This spectrum was scaled at 6825 Å to the smoothed continuum and line blocking data for the Sun of Neckel & Labs (1981) which is sampled at 50 Å intervals for 6625–8725 Å. Irradiance data for the long wavelength range 8825–9925 Å was obtained from smoothed continuum values with no lines included from the same source, sampled at 100 Å intervals. The observational mean error in the visible and infrared is reported not to exceed 1%. The data sets of Neckel & Labs (1981) were linearly interpolated to the same consecutive wavelength spacing as that of Kharitonov et al. (1988). A missing flux data point at 8775 Å was constructed from the average of 8725 and 8825 Å fluxes.

While the latter solar spectrum was used in the present analysis, no significant differences in the Mercury spectra were observed when performing calibration with the Neckel & Labs (1984) spectrum. The used solar analog spectrum is thus expected to differ in flux by at most 2% with respect to the true solar spectrum.

Calibration of Mercury spectra

The constructed calibration star and solar spectra were then linearly interpolated to 1 Å resolution and the mean fluxes for the FWHM wavelength ranges of the Ealing filters were calculated. These fluxes were normalized to the 830 nm flux, which was a common wavelength for all runs. The observed extra-atmospheric Mercury fluxes were normalized with respect to the observed flux in the 830 nm filter. Thereafter, the calibration star and solar spectra were divided out to obtain the normalized disk-integrated multicolor photometric spectra of Mercury.

REFERENCES

- The Astronomical Data Center. Web address <http://adc.gsfc.nasa.gov/>.
- Blewett, D.T, Lucey, P.G., Hawke, B.R, Ling, G.G. and M.S. Robinson 1997. A comparison of Mercurian reflectance and spectral quantities with those of the Moon. *Icarus* **129**, 217–231.
- Blewett, D.T, Lucey, P.G., Hawke, B.R, and B.L. Joliff 1997. Clementine images of the lunar sample-return stations: Refinement of FeO and TiO₂ mapping techniques. *J. Geophys. Res.* **102** (E7), 16 319–16 325.
- Cintala, M.J. 1992. Impact-induced thermal effects in the lunar and mercurian regoliths. *J. Geophys. Res.* **97** (E1), 947–973.
- Clark, P.E., Leake, M.A. and R.F. Jurgens 1988. Goldstone radar observations of Mercury. In *Mercury* (Vilas, F., Chapman, C.R. and M.S. Matthews, Eds.), pp. 77–100. University of Arizona Press, Tucson.
- Cooper, B., Potter, A.E., Killen, R.M. and T.H. Morgan 2001. Mid-infrared spectra of Mercury. *J. Geophys. Res.*, **106** (E12), 32 803–32 814.
- Dollfus, A., Chapman, C.R., Davies, M.E., Gingerich, O., Goldstein, R., Guest, J., Morrison, D. and B.A. Smith 1978. IAU nomenclature for albedo features on the planet Mercury. *Icarus* **34**, 210–214.
- Glushneva, I.N., Kharitonov, A.V., Knyazeva, L.N., and V.I. Shenavrin 1992. Secondary Spectrophotometric standards. *Astron. Astroph. Suppl. Ser.* **92**, 1–29. (Astronomical Data Center catalog III/207).
- Glushneva, I.N., Doroshenko, V.T., Fetisova, T.S., Khruzina, T.S., Kolotilov, E.A., Mossakovskaya, L.V., Shenavrin, V.I., Voloshina, I.B., Biryukov, V.V. and L.S. Shenavrina 1998. Moscow Spectrophotometric Catalog of Stars. (Astronomical Data Center catalog III/207).
- Gradie, J.C, Veverka, J. and B.J. Buratti 1980. The effects of photometric geometry on spectral reflectance. *Lunar and Plan. Sci.* **XI**, 357–359.
- Hapke, B., Danielson, G.E, Klaasen, K. and L. Wilson 1975. Photometric Observations of Mercury From Mariner 10. *J. Geophys. Res.* **80**, 2431–2443.
- Hapke, B. 1993. *Theory of reflectance and emittance spectroscopy*. Cambridge University Press, Cambridge.
- Hapke, B. 2001. Space weathering from Mercury to the asteroid belt. *J. Geophys. Res.* **106** (E5), 10 039–10 073.
- Harmon, J.K and D.B. Campbell 1988. Radar observations of Mercury. In *Mercury* (Vilas, F., Chapman, C.R. and M.S. Matthews, Eds.), pp. 101–117. University of Arizona Press, Tucson.
- Harris, D.L. 1961. In *Planets and Satellites* vol. 3 (Kuiper, G.P. and B.M. Middlehurst, Eds.), ch. 8 "Photometry and colorimetry of planets and satellites". University of Chicago Press, Chicago.
- Irvine, W.M., Simon, T., Menzel, D.H., Pikoos, C. and A.T. Young 1968. Multicolor Photoelectric Photometry of the Brighter Planets. III. Observations from Boyden Observatory. *Astron. J.* **73**, 807–828.
- Jeanloz, R., Mitchell, D.L., Sprague, A.L. and I. de Pater 1995. Evidence for a basalt-free surface on Mercury and implications for internal heat. *Science* **268**, 1455–1457.
- Kharitonov, A.V., Tereshchenko V.M. and L.N. Knyazeva 1988. Spectrophotometric Catalogue of Stars. Alma-Ata, Nauka, p. 484 (Astronomical Data Center catalog III/202).

- Lane, A.P. and W.M. Irvine 1972. Monochromatic phase curves and albedo for the lunar disk. *Astron. J.* **78**, 267–277.
- Lucey, P.G., Taylor, G.J, and E. Malaret 1995. Abundance and Distribution of Iron on the Moon. *Science* **268**, 1150–1153.
- Lucey, P.G., Blewett, D.T., and B.R. Hawke 1998. Mapping the FeO and TiO₂ content of the lunar surface with multispectral imagery. *J. Geophys. Res.* **103** (E2), 3679–3699.
- McCord, T.B. and J.B. Adams 1972. Mercury: Surface Composition from the Reflection Spectrum. *Science* **178**, 745–746.
- McCord, T.B. and J.B. Adams 1972. Mercury: Interpretation of Optical Observations. *Icarus* **17**, 585–588.
- McCord, T.B. and R.N. Clark 1979. The Mercury soil – Presence of Fe²⁺. *J. Geophys. Res.* **84**, 7664–7668.
- Mendillo, M., Warell, J., Limaye, S.S., Baumgardner, J., Sprague, A. and J.K. Wilson 2001. Imaging the surface of Mercury using ground-based telescopes. *Planet. Space Science* **49**, 1501–1505.
- Mitchell, D.L. and I. de Pater 1994. Microwave Imaging of Mercury's Thermal Emission at wavelengths from 0.3 to 20.5 cm. *Icarus* **110**, 2–32.
- Mustard, J.F. and C.M. Pieters. 1989. Photometric phase functions of common geologic materials and applications to quantitative analysis of mineral mixture reflectance spectra. *J. Geophys. Res.* **94** (B10), 13 619–13 634.
- Neckel, H. 1986. The absolute energy distributions of the Sun, of the 'solar analogs' 16 Cyg B, Hyades VB 64, 16 Cyg A, and of the standard stars α Lyr and 29 Psc. *Astron. Astroph.* **159**, 175–188.
- Neckel, H. and D. Labs 1981. Improved data of solar spectral irradiance from 0.33 to 1.25 μm . *Solar Physics* **74**, 231–249.
- Neckel, H. and D. Labs 1984. The solar radiation between 3300 and 12500 Å. *Solar Physics* **90**, 205–258.
- Pickles, A.J. 1998. A Stellar Flux Library: 1150–25000 Å. *Publ. Astron. Soc. Pac.* **110**, 863.
- Pieters, C.M. 1983. Strength of mineral absorption features in the transmitted component of near-infrared reflected light: First results from RELAB. *J. Geoph. Res.* **88** (B11), 9534–9544.
- Pieters, C.M., Pratt, S., Hoffmann, H. Helfenstein, P. and J. Mustard 1991. Bidirectional spectroscopy of returned lunar soils: Detailed "ground truth" for planetary remote sensors. *Lunar Planet. Sci.* **XXII**, #1162, 1069–1070.
- Pieters, C.M. 1993. Compositional Diversity and Stratigraphy of the Lunar Crust Derived from Reflectance Spectroscopy. In *Remote Geochemical Analysis: Elemental and Mineralogical Composition* (C.M. Pieters and P.A.J. Englert, Eds.), pp.309–339. Cambridge University Press, Cambridge.
- Rava, B. and B. Hapke 1987. An analysis of the Mariner 10 color ratio map of Mercury. *Icarus* **71**, 397–429.
- Robinson, M. S., and P.G. Lucey 1997. Recalibrated Mariner 10 image mosaics: Implications for Mercurian volcanism. *Science* **275**, 197–200.
- Rufener, F. 1986. The evolution of atmospheric extinction at La Silla. *Astron. Astroph.* **165**, 275–286.
- Scharmer, G. 1998. Conceptual Design of a New Swedish Solar Telescope. Publ. of the Royal Swedish Academy of Sciences, Stockholm Observatory, Stockholm.

- Shkuratov, Y.G., Kaydash, V.G., Pieters, C. and N.V. Opanasenko 1999. A comparison of absolute calibrations of Clementine-UVVIS and Earth-based data for the Moon. *Lunar Planet. Sci.* **XXX**, #1165, 1130–1131.
- Shkuratov, Y., Starukhina, L., Hoffmann, H. and G. Arnold 1999. A Model of Spectral Albedo of Particulate Surfaces: Implications for Optical Properties of the Moon. *Icarus* **137**, 235–246.
- Sprague, A.L., Koslowski, R.W.H., Witteborn, F.C., Cruikshank, D.P. and D.H. Wooden 1994. Mercury: Evidence for Anorthosite and Basalt from Mid-infrared (7.3–13.5 μm) Spectroscopy. *Icarus* **109**, 156–167.
- Sprague, A.L., Nash, D.B., Witteborn, F.C. and D.P. Cruikshank 1997. Mercury’s feldspar connection: Mid-IR measurements suggest plagioclase. *Adv. Space Res.* **19**, 1507–1510.
- Sprague, A.L., Schmidt, W.J. and R.E. Hill 1998. Mercury: Sodium Atmospheric Enhancements, Radar-Bright Spots, and Visible Surface Features. *Icarus* **136**, 60–68.
- Sprague, A.L., Deutsch, L.K., Hora, J., Fazio, G.G., Ludwig, B., Emery, J. and W.F. Hoffmann 2000. Mid-infrared (8.1–12.5 μm) Imaging of Mercury. *Icarus* **147**, 421–432.
- Starukhina, L. 2001. Water detection on atmosphereless celestial bodies: Alternative explanations of the observations. *J. Geoph. Res.* **106** (E7), 14 701–14 710.
- Starukhina, L. and Y.G. Shkuratov 2001. A Theoretical Model of Lunar Optical Maturation: Effects of Submicroscopic Reduced Iron and Particle Size Variations. *Icarus* **152**, 275–281.
- Stationary Office, The. 2000. *The Astronomical Almanac 2000*. U.S. Government Printing Office, Washington, D.C..
- Sterken, C. and J. Manfroid 1992. *Astronomical Photometry: A Guide*. Kluwer Academic Publishers, Dordrecht.
- Veverka, J., Helfenstein, P., Hapke, B. and J. Goguen 1988. In *Mercury* (Vilas, F., Chapman, C.R. and M.S. Matthews, Eds.), pp. 37–58. University of Arizona Press, Tucson.
- Vilas, F. and T.B. McCord 1976. Mercury: Spectral reflectance measurements (0.33–1.06 μm) 1974/75. *Icarus* **28**, 593–599.
- Vilas, F., Leake, M.A. and W.W. Mendell 1984. The dependence of Reflectance Spectra of Mercury on Surface Terrain. *Icarus* **59**, 60–68.
- Vilas, F. 1985. Mercury: Absence of Crystalline Fe^{2+} in the Regolith. *Icarus* **64**, 133–138.
- Vilas, F. 1988. Surface composition of Mercury from reflectance spectrophotometry. In *Mercury* (Vilas, F., Chapman, C.R. and M.S. Matthews, Eds.), pp. 59–76. University of Arizona Press, Tucson.
- Warell, J. and S. Limaye 2000. Properties of the Hermean Regolith: I. Global regolith albedo variation at 200 km scale from multicolor CCD imaging. *Planet. Space Science* **49**, 1531–1552.

This 2-column preprint was prepared with the AAS L^AT_EX macros v4.0.

TABLE 1
GEOMETRIC ALBEDO OF MERCURY

λ	A_p
550	0.138 ^a
650	0.160 ^b ±0.005 ^c
753	0.188 ^d ±0.008 ^c
833	0.208 ^d ±0.010 ^c
944	0.240 ^d ±0.014 ^c

^aGeometric albedo from Veverka et al. (1988)

^bAlbedo value determined from the spectral slope of Vilas (1984) and 550 nm geometric albedo

^cAll error bars from this work

^dAlbedo value determined from spectral slope of this work

TABLE 2
FEATURES SELECTED FOR MULTICOLOR PHOTOMETRY ON MERCURY DISK IMAGES. LOCATION IS RELATIVE TO NAMED FEATURES ON THE OFFICIAL IAU ALBEDO MAP (DOLLFUS ET AL. 1978).

SVST #	Longitude	Latitude	e (°)	α (°)	Date	Hue	IAU location
a	170	-10	-53	63	1997 Nov 24	Dark	Sol. Helii
34	171	+11	-52	63	1997 Nov 24	Light	Central Heliocaminus
42	193	-6	-30	63	1997 Nov 24	Light	NW of Sol. Helii, NE of Sol. Atlantis
44	200	+32	-39	63	1997 Nov 24	Light	SW Liguria; within Caloris basin
b	210	+10	-17	63	1997 Nov 24	Dark	SE Sol. Phoenicis
c	210	-40	-40	63	1997 Nov 24	Dark	Sol. Atlantis
48	219	-22	-20	63	1997 Nov 24	Light	N of Sol. Atlantis
d	230	+30	+33	63	1997 Nov 24	Dark	Central Sol. Phoenicis
52	242	+10	+23	63	1997 Nov 24	Light	N of Sol. Criophori
52	242	+10	+65	84	1998 Jul 9	Light	N of Sol. Criophori
e	260	0	+47	84	1998 Jul 9	Dark	NW of Sol. Criophori
56	265	+16	+43	84	1998 Jul 9	Light	NW of Sol. Criophori, SE of Sol. Aphrodites
f	265	-30	+53	84	1998 Jul 9	Dark	SW Sol. Criophori
57	266	+31	+47	84	1998 Jul 9	Light	NE of Sol. Aphrodites
64	289	+3	+18	84	1998 Jul 9	Light	E of Pentas
66	293	+40	+36	84	1998 Jul 9	Light	N of Sol. Aphrodites
g	300	+20	+16	84	1998 Jul 9	Dark	W Sol. Aphrodites
h	300	-10	+17	84	1998 Jul 9	Dark	SE of Pentas, NW of Sol. Alarum

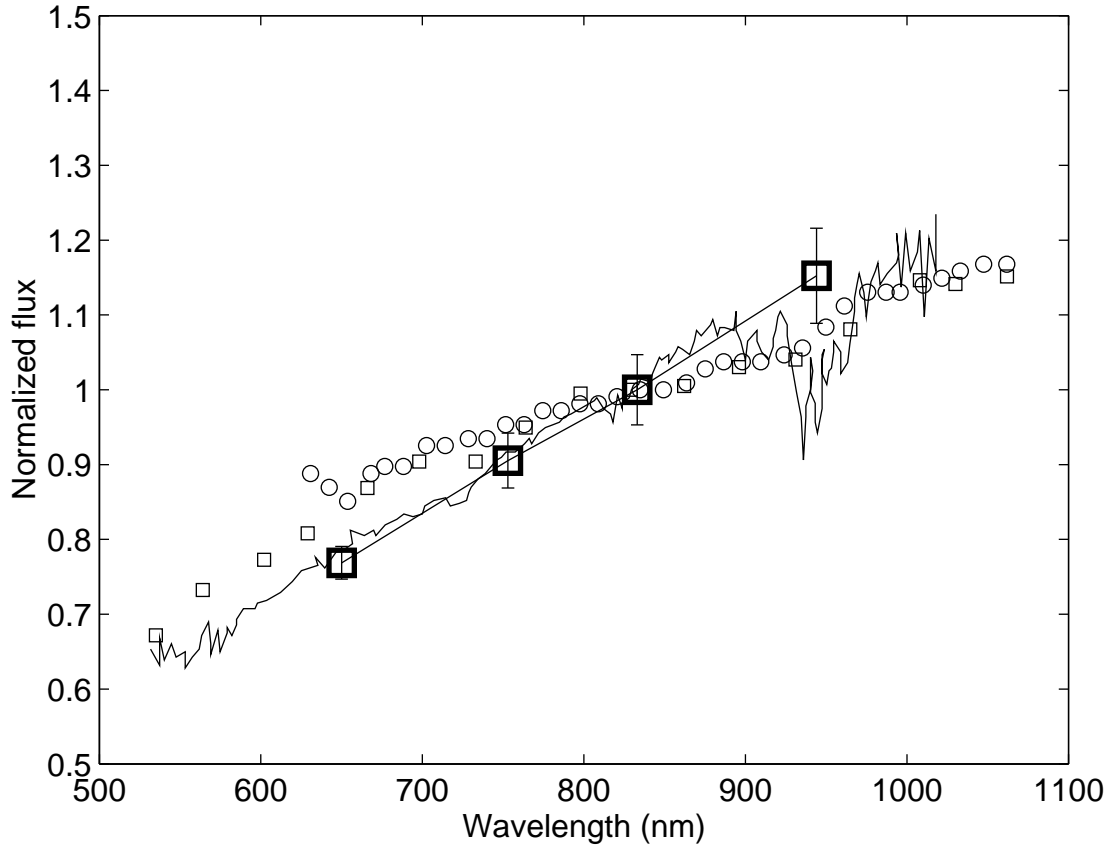


Fig. 1.— Disk integrated photometry of Mercury from SVST image data (squares), compared with spectrophotometry from 5–7 October 1974 (Vilas et al. 1984; limb–terminator longitudes 144° – 235° ; squares), 21 April 1976 (McCord & Clark 1979; limb–terminator longitudes 168° – 270° ; circles) and a CCD spectrum obtained on 24 November 1984 (Vilas 1985; limb–terminator longitudes 147° – 255° ; solid line). All spectra have been scaled to unity at a wavelength of 830 nm. The SVST photometry is an arithmetic average of data from 22 November 1997 and 7 and 9 July 1998. The 1997 data is centered on the Caloris basin (limb–terminator longitudes 124 – 244°), while the 1998 data covers the eastern part of the poorly known hemisphere (limb–terminator longitudes 208 – 313°). The phase angles of Mercury for these dates are 58.6° , 80.4° and 84.0° , respectively.

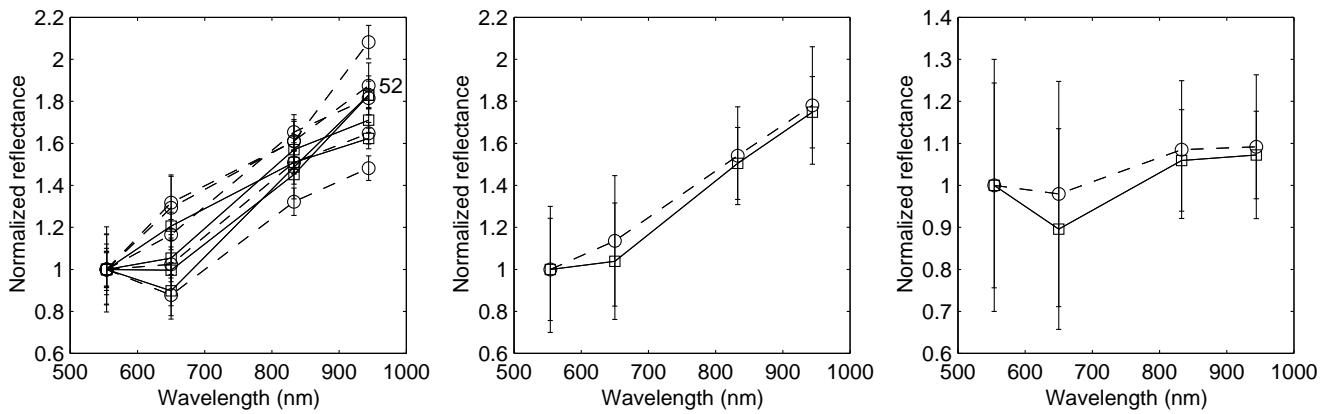


Fig. 2.— Multicolor photometry of mercurian albedo features from disk images obtained on November 24, 1997. All spectra are normalized to unity at 550 nm. Left panel: Flux in each measured feature. Bright feature spectra are shown as circles and dashed lines, dark features as squares and solid lines. The bright feature SVST #52 which is measured also in 1998 has been identified. Central panel: Average spectra of bright and dark features. Right panel: Averaged spectra of bright and dark features divided by the Mercury integrated disk spectrum (Fig. 1).

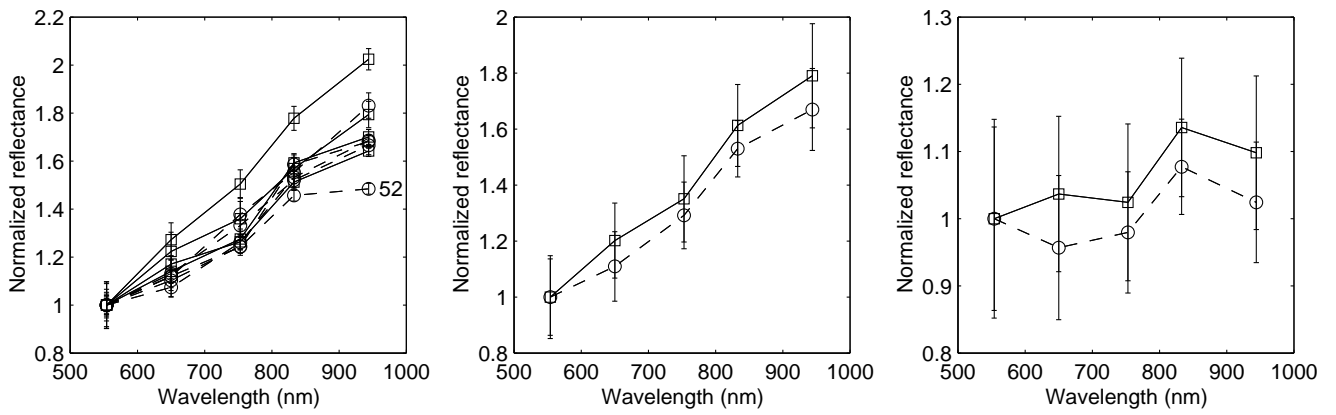


Fig. 3.— Multicolor photometry of mercurian albedo features from disk images obtained on July 9, 1998. See caption of Fig. 2 for details.

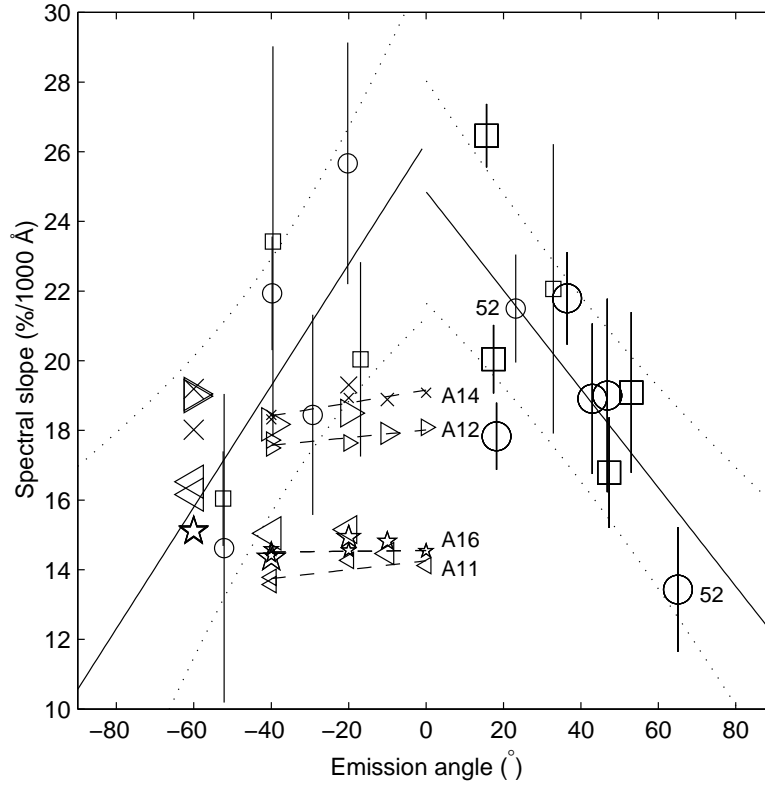


Fig. 4.— Spectral slopes for mercurian albedo features as a function of emission angle. Squares are measurements for dark features, circles for bright features. Small symbols are for measurements at a phase angle of 63.4° (1997 November 24) at which the emission angles were negative (i.e., $g > |i|$) for the majority of locations. Large symbols are for a phase angle of 84.0° (1998 July 9) at which most emission angles were positive. Error bars represent one sigma ranges from linear fits to individual feature spectra in the interval 550–940 nm. The solid lines are the best linear fits for the two separate data sets and are seen to be identical within error limits (50% confidence envelopes are defined by dotted lines). The relation is furthermore identical for bright and dark features at the current spatial resolution. Stars, crosses, right-pointing triangles and left-pointing triangles are "continuum" slopes for the wavelength range 550–750 nm obtained from Pieters et al. (1991) laboratory spectra of lunar soil samples collected by Apollo 16, 14, 12 and 11, respectively, sampled at the same wavelengths as the SVST data. Increasing sizes of these data points denote increasing phase angle in the order of 60° , 70° , 80° and 100° . Linear fits for a phase angle of 60° are shown as dashed lines for highland samples (Apollo 14 and 16) and mare samples (Apollo 11 and 12). Bright mercurian feature #52, observed at both phase angles, is marked. It occupies two locations on one of the branches of the slope–emission angle relation and is most probably travelling along the two branches as the emission angle is varied. It may be assumed that it represents the photometric behaviour of a typical location on the mercurian surface.

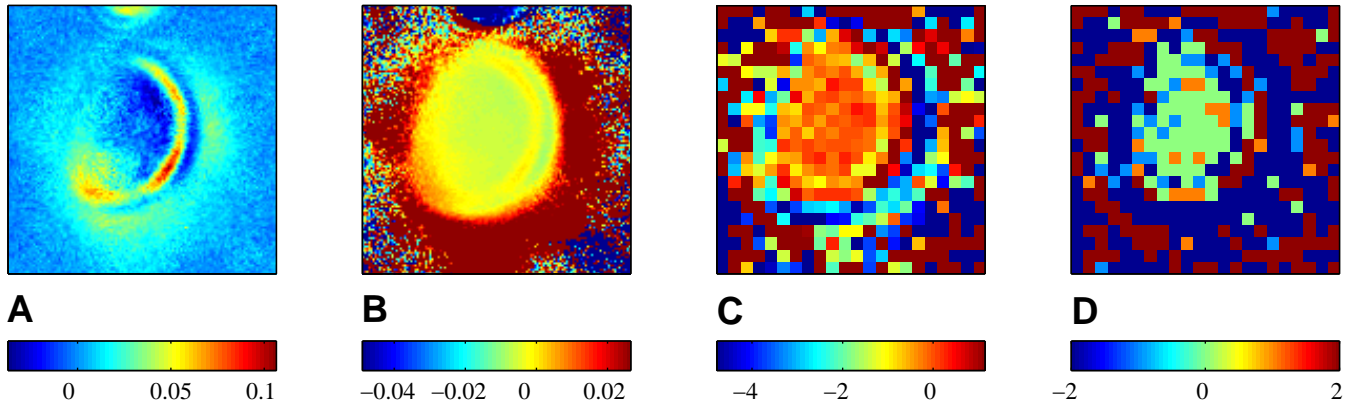


Fig. 5.— Color variation on Mercury on 1997 October 22. Pseudocolor bars display the pixel intensities of the images. In panel A, a 550 nm image has been smeared by a 5×5 pixel boxcar filter (true for all panels) and subtracted from a 940 nm image, each of which were previously normalized to a maximum intensity of unity and a mean sky level of zero. Panel B shows the ratio 940 nm/550 nm. The integrated disk flux of each input image was previously set to the proper geometric albedo. Panel C is a relative intensity map R . Each of the input image pixels have been binned 5×5 , then the same ratio as in panel B formed, followed by calculating the difference in percent of each pixel intensity from the mean of the four closest neighbors. In panel D the R map intensities are converted to standard deviations from the mean intensity in a 5×5 pixel box at the center of the disk, forming a variation map V . No on-disk pixels deviate in intensity by more than 1σ ($\sim 1\%$) from their neighbors, providing negative evidence for a spatial variation of pyroxene band strength at a mid-disk spatial resolution of 260 km. Imaged longitudes are $124\text{--}244^\circ$, primarily on the poorly known hemisphere. Results from smearing by a Gaussian filter are very similar.

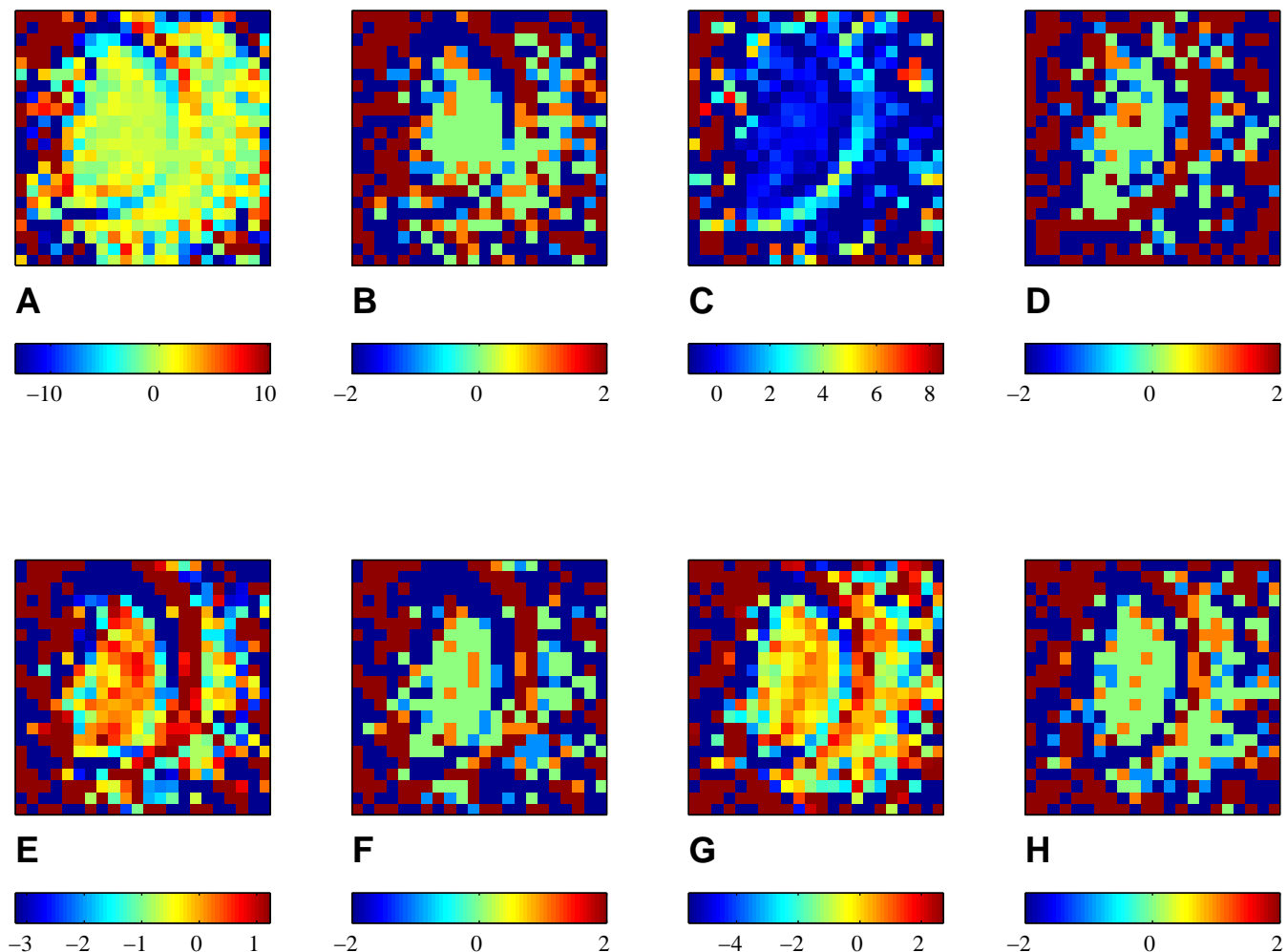


Fig. 6.— Color variation on Mercury on 1998 July 9 for four ratio images. Panels A, C, E and G are R maps, other panels are V maps, as described in the caption for Fig. 5. Panels A and B are the results of forming a 650 nm/550 nm ratio with the denominator image smeared by a 2×2 boxcar filter. Panels C and D are similar 830 nm/550 nm ratios using a 3×3 boxcar filter, panels E and F are 940 nm/550 nm ratios using a 4×4 boxcar filter and panels G and H are 940 nm/550 nm ratios formed from another pair of input images, with the denominator image smeared by a 2×2 boxcar filter. No on-disk pixels deviate in intensity by more than 1σ ($\sim 1\%$) from their neighbors in the 940 nm/550 nm maps. This provides negative evidence for a spatial variation of pyroxene band strength at a mid-disk spatial resolution of 230 km. Imaged longitudes are in the range $217\text{--}313^\circ$, located on the poorly known hemisphere.